

Automation of finding strong gravitational lenses in the Kilo Degree Survey with U - DenseLens (DenseLens + Segmentation)

Bharath Chowdhary N ¹, Léon V.E. Koopmans ¹, Edwin A. Valentijn ¹, Gijs Verdoes Kleijn ¹, Jelte T. A. de Jong ¹, Nicola Napolitano ^{2,3,5}, Rui Li ^{4,6}, Crescenzo Tortora ², Valerio Busillo ², Yue Dong ⁷

¹Kapteyn Astronomical Institute, University of Groningen, PO Box 800, NL-9700 AV Groningen, the Netherlands

²INAF – Osservatorio Astronomico di Capodimonte, Via Moiariello 16, I-80131 Napoli, Italy

³School of Physics and Astronomy, Sun Yat-sen University, Zhuhai Campus, 2 Daxue Road, Xiangzhou District, Zhuhai, China

⁴School of Astronomy and Space Science, University of Chinese Academy of Sciences, Beijing 100049, China

⁵CSST Science Center for Guangdong-Hong Kong-Macau Great Bay Area, Zhuhai, 519082, China

⁶National Astronomical Observatories, Chinese Academy of Sciences, 20A Datun Road, Chaoyang District, Beijing 100012, China.

⁷Xi'an Jiaotong-Liverpool University, Wuzhong District, Suzhou, China, 215000.

Accepted XXX. Received YYY; in original form ZZZ

ABSTRACT

In the context of upcoming large-scale surveys like Euclid, the necessity for the automation of strong lens detection is evident. While existing pipelines heavily rely on the classification probability (P), this study underscores the importance of integrating additional metrics, such as Information Content (IC) and the number of pixels above the segmentation threshold (n_s), to address the false positive rate in unbalanced datasets. This research introduces a segmentation algorithm (U-Net) as a supplementary step in the established strong gravitational lens identification pipeline (DenseLens), which primarily utilizes P_{mean} and IC_{mean} for detection and ranking. The results demonstrate that the inclusion of segmentation allows for a significant reduction of approximately 25% in the final sample extracted from DenseLens, without compromising the identification of strong lenses. The main objective of this study is to automate the strong lens finding process by integrating these three metrics. To achieve this, a decision tree-based selection process is introduced, applied to both Bright Galaxy (BG) and Luminous Red Galaxy (LRG) samples. This process involves rank-ordering based on classification scores, filtering based on Information Content (IC), and segmentation score (n_s). Additionally, the study presents four newly discovered strong lensing candidates identified by the U-DenseLens network using the KiDS DR4 data.

Key words: gravitational lensing: strong < Physical Data and Processes – Cosmology

1 INTRODUCTION

Strong Gravitational Lensing is the result of the deflection of light from a distant source by a massive foreground object, resulting in multiple (resolved) images, arcs or rings based on the nature of the source and alignment. Strong lensing has many applications such as (i) study the mass distribution of galaxies (Koopmans 2004; Nightingale et al. 2019; Turyshev & Toth 2022), (ii) measure the Hubble constant H_0 using time delays between multiple resolved images (Rhee 1991; Kochanek 2003; Grillo et al. 2018; Treu et al. 2022; Treu & Shajib 2023), (iii) provides constraints of dark energy (Sarbu et al. 2001; Sereno 2002; Meneghetti et al. 2005; Biesiada 2006; Oguri et al. 2008a) and dark matter (Gilman et al. 2019; Nadler et al. 2021) in the Universe, (iv) constrain the slope of inner mass density profile (for e.g., Treu & Koopmans 2002; Zhang 2004; Gavazzi et al. 2007; Koopmans et al. 2009; Zitrin et al. 2012; Spinelli et al. 2015; Li et al. 2018; He et al. 2020a; Sengül & Dvorkin 2022), (v) provide constraints on cosmological parameters with lens statistics (Turner et al. 1984; Chae et al. 2002, 2004; Mitchell et al. 2005), (vi) to act

as natural telescopes to study magnified images of distant galaxies (Ellis 2010; Treu & Ellis 2015; Barnacka 2018).

Many strong lenses have been discovered by ground-based and space-based surveys. Space-based surveys such as the Sloan Lens ACS (SLACS) survey (Bolton et al. 2006a, 2008; Shu et al. 2015, 2017), found up to a few hundred galaxy-galaxy strong lenses using snapshot imaging survey of Hubble Space Telescope (HST). Gavazzi et al. (2008) discovered a double Einstein ring around a gravitational lens using the SLACS survey. Upcoming space-based surveys such as the Nancy Grace Roman Space telescope (previously WFIRST; Wang et al. 2022) is expected to find 17000 strong lens (Weiner et al. 2020). Several thousand strong lenses have also been found in ground based surveys such as (i) the Kilo Degree Survey (KiDS; de Jong et al. 2013) by Petrillo et al. 2017, 2019a,b, Pearson et al. 2018, Davies et al. 2019, Metcalf et al. 2019, Li et al. 2020, 2021, He et al. 2020b, (ii) The Canada-France-Hawaii Telescope Lensing Survey (CFHTLens; Heymans et al. 2012) by Cabanac, R. A. et al. 2007, More et al. 2012, 2015, Gavazzi et al. 2014, Sygnet, J. F. et al. 2010, Jacobs et al. 2017, Chan et al. 2015, (iii) The Hyper Suprime-Cam

Survey (Miyazaki et al. 2012) by Shu, Yiping et al. 2022, More et al. 2016, Chan et al. 2016, Tanaka et al. 2016, Cañameras, R. et al. 2021, Wong & HSC SSP Strong Lens Working Group 2018, Jaelani et al. 2020, (iv) VST Optical Imaging of the CDFS and ES1 fields (VOICE; Gentile et al. 2021), (v) Dark Energy Survey (DES; Collaboration 2005) by Rojas et al. 2021, Treu et al. 2018, Diehl et al. 2017, Treu et al. 2018, Anguita et al. 2018, Agnello et al. 2015, Huang et al. 2020, Nord et al. 2015; Nord et al. 2016, 2020, O’Donnell et al. 2022, Lemon et al. 2020.

Strong lenses have also been found with other techniques such as (i) radio imaging based Cosmic Lens All-Sky Survey (CLASS; Myers et al. 2001) by Browne et al. 2003; Myers et al. 1999, (ii) SDSS Quasar Lens Search (SQLS; Oguri et al. 2006, 2008b) using spectroscopy method by Bolton et al. 2006b; Belokurov et al. 2009; Oguri et al. 2005 and Inada et al. 2014, (iii) u-band based search with Canada France Imaging Survey (CFIS; Ibata et al. 2017) using multi-band Ultraviolet Near Infrared Optical Northern Survey (UNIONS; Savary et al. 2021, 2022)

The number of galaxy-scale strong lens candidates will increase by three orders of magnitudes with upcoming large-scale sky surveys. 10^5 strong lenses are expected to be discovered (e.g., Serjeant 2014, Pawase et al. 2014, Collett 2015) by upcoming large scale sky surveys such as the Large Synoptic Survey Telescope, LSST; Tyson 2002), Euclid (Laureijs et al. 2010), the Square Kilometer Array (SKA; Dewdney et al. 2009, Quinn et al. 2015; Koopmans et al. 2004) and the Chinese Space Station Telescope (CSST; Zhan 2018). Using human volunteers as classifiers becomes increasingly difficult (next to impossible) with these upcoming surveys. Davies (2022) showed that human classifiers were less successful when compared with the Convolutional Neural Network (hereafter CNN) at classifying strong lenses when subjected to a classification task in a Zooniverse (Simpson et al. 2014) project. CNNs have also been greatly preferred after showing promising results in the strong gravitational lens finding challenge (Metcalf et al. 2019).

A Convolutional Neural Network (CNN; Lecun et al. 1998) is an adaptive learning algorithm that learns the features of images utilizing spatial hierarchy through gradient-based backpropagation. Owing to its efficiency, CNNs have been largely preferred over other machine learning techniques (such as SVM, ResNets, AlexNets) and have been widely used in recent research methodologies (Petrillo et al. 2017, 2019a,b, Pearson et al. 2018, Lanusse et al. 2018, Pourrahmani et al. 2018, Schaefer et al. 2018, Davies et al. 2019, Metcalf et al. 2019, Li et al. 2020, 2021, Cañameras et al. 2020, Christ et al. 2020 and Rezaei et al. 2022) to find strong lenses. However, due to the highly unbalanced nature of the dataset and the close resemblance of some classes of non-lenses with lens candidates, a large number of false positives in the final sample cannot be avoided. Therefore, we propose the usage of segmentation techniques in addition to CNNs to lower the rate of false positives.

Segmentation is a technique where select pixels of the image are classified into one or many classes. Some of the popular segmentation architectures include Faster R-CNN (Ren et al. 2015), Mask R-CNN (He et al. 2017), Segnet (Badrinarayanan et al. 2017) and U-Net (Ronneberger et al. 2015). Faster R-CNN has been used in the morphology classification of radio sources (Wu et al. 2018), detection of L-Dwarfs (Cao et al. 2023), detection and classification of astronomical targets (Jia et al. 2020), detection of supernovae (Guo et al. 2021; Wu 2020). Mask RCNN, a successor of Faster R-CNN, has been used in the morphological segmentation of galaxies (Farias et al. 2020; Gu et al. 2023), to detect, classify and deblend astronomical sources (Burke et al. 2019), to detect and classify sources in radio continuum images (Riggi et al. 2023) and to detect and mask ghosting

and scattered-light artifacts from optical survey images (Tanoglidis et al. 2022).

Segmentation with U-Net was first proposed by Ronneberger et al. (2015) for medical image segmentation. Since then, it has been widely used in various fields. In radio astronomy U-Net has been to classify clean signal and RFI signatures (Akeret et al. 2017), automatic recognition of RFI (Long et al. 2019). U-net has also been used to segment spiral arms of disk galaxies (Bekki, K. 2021) and denoising astronomical images (Qi et al. 2022; Vojtekova et al. 2020).

In the field of strong lensing, U-Net has been used for segmenting dark substructure (subhalos; Ostdiek, Bryan et al. 2022a), to segment blended galaxy pairs (Boucaud et al. 2019), to measure subhalo mass function (SMF; Ostdiek, Bryan et al. 2022b), to find quadruply imaged quasars (Akhazhanov et al. 2022) and to generate neutrino simulations (Giusarma et al. 2019).

In the case of extensive surveys like Euclid, which entail the analysis of millions of candidates, the post-processing results from the Denselens pipeline can still yield thousands of candidates requiring daily vetting. To address this problem, we propose a novel idea of using segmentation algorithm (U-Net) to segment source pixels of the strong lensing candidates. Typically, U-Net is favored over alternative versions of R-CNN due to its lighter model structure (fewer parameters), while maintaining comparable efficiency for semantic segmentation tasks (Widyaningrum et al. 2022). We use U-Nets in addition to the DenseLens (Nagam et al. 2023) network (implemented in our previous paper) to classify strong lenses and to reduce false positives in the final sample. In Sec. 2 we describe the KiDS datasets used for classification and rank-ordering. In Sec. 3 we describe the methodology to segment source pixels.

2 DATA SETS

Kilo Degree Survey (KiDS) is an wide-field optical imaging survey operating with a 268 million pixel square CCD mosaic camera (OmegaCAM; Kuijken et al. 2011) mounted on the VLT-Survey Telescope (VST; Capaccioli & Schipani 2011) at ESO’s Paranal observatory in Chile. The KiDS survey is the deepest of the three wide area public imaging surveys ever conducted with best observing conditions. KiDS observes around 1350 square degrees of extragalactic sky in four filters (u,g,r,i). r-band images have the best seeing condition with the median Point Spread Function (PSF) FWHM of <0.7 arcsec and an exposure time of 1800 seconds. In this paper, we utilize the data from 904 tiles from KiDS DR4 data release (Kuijken et al. 2019). We have used ~ 3.8 million r-band cutouts of size 101×101 pixels which corresponds to the area of 20×20 arcseconds².

2.1 Data selection

We present a detailed account of the methodology employed in creating KiDS cutouts, outlined below. Our study exclusively utilizes r-band images, with g, r, i images showcased solely for illustrative purposes. Our approach is similar with the methodology introduced by Li 2020 and Petrillo et al. 2019a.

1. BG Sample: We employ two criteria for selecting KiDS cutouts: (i) Setting the parameter SG2DPHOT to 0 to exclusively target galaxies. SG2DPHOT is a flag generated by the automated tool 2DPHOT (Barbera et al. 2008), offering both integrated and surface photometry for galaxies within an image. Employing Sextractor (Bertin & Arnouts 1996), we generate cutouts using r-band *mag_auto* with the constraint $r_{\text{auto}} \leq 21$. This yields approximately 3.8 million cutouts under this criterion.

2. LRG Sample: We focus on selecting Luminous Red Galaxies (LRGs) with redshifts (z) less than 0.4. This involves isolating areas in (r-i) and (g-r) color diagrams based on the following criteria:

$$\begin{aligned} |c_{\text{perp}}| &< 0.2, \\ r &< 14 + c_{\text{par}}/0.3 \end{aligned} \quad (1)$$

where,

$$\begin{aligned} c_{\text{par}} &= 0.7(g - r) + 1.2[(r - i) - 0.18], \\ c_{\text{perp}} &= (r - i) - (g - r)/4.0 - 0.18. \end{aligned}$$

This selection criterion results in approximately 126,000 LRG cutouts.

3 METHODOLOGY

In our prior research presented in DenseLens (Nagam et al. 2023), we introduced a pioneering approach for the classification and rank-ordering of strong gravitational lenses. To enhance accuracy and lower false positives, we introduce an integrated approach, U-DenseLens, which combines DenseLens with a U-Net segmentation network. In the subsequent Sec. 3.2, we delve into the application of U-Net for pixel segmentation within input lens candidate images, providing a detailed methodology for training and classification. The synergistic integration of DenseLens and U-Net segmentation aims to refine our model's accuracy in identifying strong lens candidates.

3.1 DenseLens

In our preceding publication, DenseLens (Nagam et al. 2023), we demonstrated the application of classification and regression ensembles for the purpose of classifying and rank-ordering strong lenses. Upon providing an input image to the DenseLens algorithm, four densely connected networks generate classification scores within the range of 0 to 1. The mean of these scores (P_{mean}) is subsequently computed. To filter out candidates with P_{mean} values falling below a designated threshold (P_{thres}), typically set as a large value, a filtering process is implemented.

We also explain in the paper about the Information content (IC), which aids in ranking images based on the number of resolution elements in noise-less mock lensed images above a brightness threshold, relative to background noise (σ). It scales with the ratio of this area to the PSF area, multiplied by the ratio of the Einstein radius (R_E) to the effective source radius (R_{eff}), preventing bias towards certain lens characteristics. The images that survive this filtering are then fed into regression networks which are trained to predict IC. The resultant mean of the outputs from these regression networks is denoted as IC_{mean} . The filtered candidates are then systematically rank-ordered based on the computed IC_{mean} values.

3.2 Segmentation

To further reduce false positive rates, we introduce an additional segmentation network at the end of the DenseNet pipeline. This augmented configuration, comprising DenseLens and the U-Net segmentation network, is termed as *U-DenseLens*. This integrated approach aims to further refine the accuracy of our model by leveraging the capabilities of U-Net segmentation in the identification of

strong lens candidates.

The U-Net architecture, initially developed for biomedical image segmentation Ronneberger et al. (2015), has become a widely adopted tool in various applications. In this study, we employ U-Net for segmenting source pixels within input lens candidate images. Specifically, for lenses, our training approach designates all source pixels as 1 and other pixels as 0. Conversely, for non-lenses, all pixels are trained with a label of 0. A detailed explanation of this methodology is provided in Appendix A.

The U-Net architecture used in this paper is illustrated in Figure 1. In our model, we employ interpolation to resize the initial 101×101 pixel input image to a 256×256 pixel configuration. Subsequently, this resized image undergoes processing through the UNet architecture. The resulting output from the U-Net model comprises 101×101 pixels, with each pixel exhibiting values in the range of 0 to 1. A notable modification involves employing a sigmoid activation function Narayan (1997) for the final layer. This modification ensures that each pixel obtained as output in the final layer possesses values within the range of 0 to 1. To classify source pixels, we set the segmentation threshold (S_{thres}) to 0.6. In Figure 10, we illustrate the results of a segmentation model where pixel values range from 0 to 1. To selectively consider only pixels corresponding to the source in the original images, we adjusted the segmentation threshold (S_{thres}) to 0.6, effectively filtering out irrelevant pixels. This threshold variation enabled precise identification and counting of source pixels, enhancing the accuracy of our segmentation outcomes. Consequently, pixels with $S_{\text{thres}} \geq 0.6$ are categorized as source pixels. The total count of classified source pixels (n_s) is determined using this threshold.

We experimented with mock lenses which were produced with brightness scaling factors and Sérsic parameters. Across these experiments, we systematically investigated diverse threshold values to effectively categorize candidates. This classification included easily identifiable lenses (Sure lens), candidates devoid of source pixels (Non-lens), and those falling within intermediate classifications (Maybe lens). This experimentation lead us to define the following scheme:

$n_s \geq 40$	<i>Sure lens (green)</i>
$n_s > 0$ and $n_s < 40$	<i>Maybe lens (yellow)</i>
$n_s = 0$	<i>Non-lens (red)</i>

We collect the output (n_s) obtained from the segmentation process with the additional outputs derived from DenseLens, namely P_{mean} and IC_{mean} . This collective information is utilized to classify and establish a rank order for strong gravitational lenses. By leveraging multiple outputs, our approach aims to enhance the robustness and accuracy of the classification and ranking process.

4 RESULTS

In this section, we systematically generated mock data and we apply our U-DenseLens model to the mock data and we explain the results in Sec. 4.1. We further apply our network and we develop a decision tree based automation technique to BG sample and show the results in Sec. 4.2. This selection is validated through a voting mechanism with

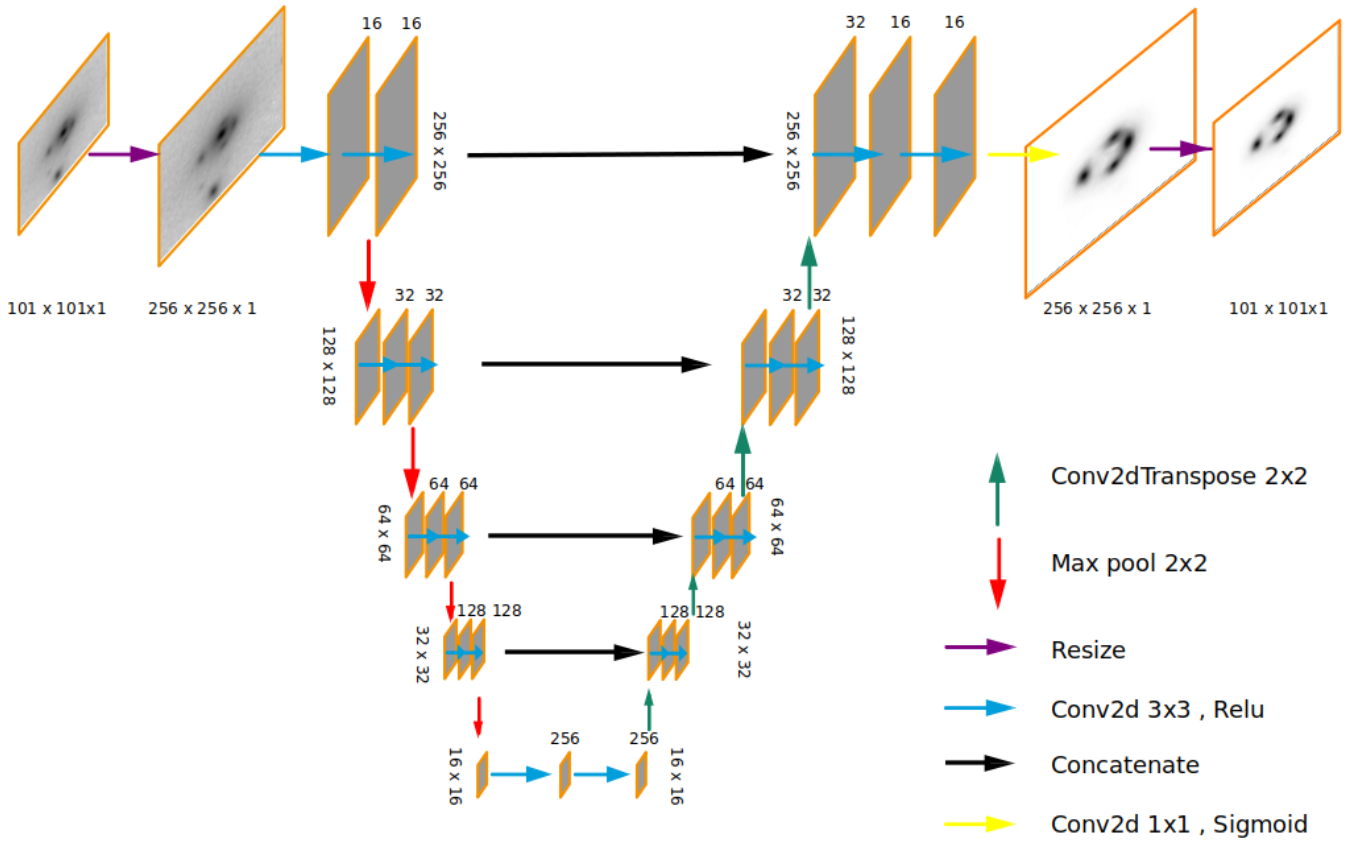


Figure 1. Description of UNet architecture used in this paper. Thus the final output obtained from the U-net model has 101×101 pixels with each pixel varying between 0 to 1. In our model, we resize our input image of 101×101 pixels into the shape of 256×256 pixels through interpolation. Then the image is passed through the U-Net architecture as shown in the Figure 1.

human classifiers, emphasizing the agreement of decision tree results with human classifier votes. Our results demonstrate the efficacy of the proposed approach, offering insights into the reduction of false positives without compromising genuine strong lensing candidates. Additionally, we extended our analysis to the LRG sample in Sec. 4.3, revealing the versatility and generalizability of our decision tree in optimizing the selection process for diverse datasets.

4.1 Mock data

We generated the mock data as detailed in Nagam et al. (2023), comprising of 10000 lens and 10000 non-lenses. We aim to investigate the impact of segmentation on both classes of mock samples. To achieve this, we deliberately set the threshold parameter (P_{thres}) at a low value of 0.3. This choice was made to minimize the extent of filtering applied during the classification prediction (P), allowing us to observe the nuanced effects of segmentation on the mock sample classes. Following classification with a very low threshold score of $P_{\text{thres}} > 0.3$, We identified 9586 candidates as lens candidates and 875 candidates as non-lens candidates. The distribution of candidates is explained in Table 1 for lenses and Table 2 for non-lenses. Notably Table 2 reveals that 77% of non-lens candidates surpassing the P_{thres} fall into the *Red* category ($n_s=0$). In contrast, only 14% of the lens candidates share the same categorization. This implies that by excluding candidates in the *Red* category, we can eliminate 77% of false positives, but at the cost of potentially discarding 14% of true

TABLE 1: Lens

	Count	%
$n_s \geq 40$	1342	14
$n_s > 0 \& n_s < 40$	4732	49
$n_s = 0$	3512	37

TABLE 2: Non-Lens

	Count	%
$n_s \geq 40$	674	77
$n_s > 0 \& n_s < 40$	201	23
$n_s = 0$	0	0

lenses.

It is essential to note that, in this scenario, lenses and non-lenses are evenly distributed in a 1:1 ratio. In practical astronomical datasets, this ratio can significantly differ, potentially reaching ratios such as 1:1000. For instance, in a real-world scenario with 10^5 non-lenses, one might expect to find around 100 lenses. The trade-off between false positives and potential loss of true positives underscores the importance of carefully adjusting classification thresholds, particularly in imbalanced datasets.

4.2 BG sample

We have devised a decision tree to reduce the false positives in the final sample (also explained as flow diagram in Figure 3). This constitutes our decision tree for the selection of strong gravitational

lenses:

(i) Rank-order candidates based on P:

We initiate the selection process by rank-ordering candidates according to their classification scores (P).

(ii) Filtering candidates with IC<=50:

Candidates characterized by an IC less than or equal to 50 are filtered out in this step. This strategic filtering step is crucial to exclude candidates exhibiting thick blob like structures. [Figure 2](#) illustrates the top-12 candidates that fall within this category. Notably, these candidates often present challenges in differentiation due to presence of dense central structures, making them indistinguishable as lenses (except for the first candidate). Despite their high P values and elevated ranks, the necessity to eliminate candidates with IC values less than or equal to 50 is apparent.

(iii) Remove candidates with $n_s = 0$ and IC<=100:

Subsequent to the IC-based filtration, candidates with zero classified source pixels (n_s) and IC values less than or equal to 100 are removed. This additional step ensures a refined selection process by removing the candidates that are completely rejected by the U-Net segmentation algorithm.

Throughout this paper, we consistently use the term "Human classifiers" to collectively refer to the eight authors involved in this study. This group was tasked with evaluating the top 1000 candidates, which were rank-ordered based on P_{mean} , from the BG sample comprising of ~3.8 million candidates. Each member of the human classifiers systematically voted on all candidates, utilizing a set of predefined options. Notably, each option is associated with a corresponding score as detailed below.

<i>Sure lens</i>	1
<i>Maybe lens</i>	0.7
<i>Maybe Non-lens</i>	0.3
<i>Non-lens</i>	0

With a vast dataset sample comprising approximately 3.8 million cutouts from the BG dataset, we selected the top 1000 candidates based on the P_{mean} criterion. The distribution of candidates in red, yellow, green, and blue (explained shortly) categories yielded 260, 488, 206, and 46 candidates, respectively. Thus we could argue that if we remove these 260 candidates with $n_s=0$ (red) as false positives, we can potentially reduce the false positives in the final sample by 26% without human culling. However, prior to this removal, it is necessary to ensure the exclusion of only false positives and not genuine candidates. Consequently, we undertook a validation process, automating the identification of strong lenses through a voting mechanism involving human classifiers.

The top 1000 candidates were presented to human classifiers in a randomized, label-free manner to eliminate any potential bias. The voting results, plotted against P_{mean} , are depicted in [Figure 4](#) (left). Candidates democratically selected by obtaining votes of either "lens" (1) or "maybe-lens" (0.7) from four or more human classifiers are showcased in [Figure 4](#) (right). While aiming to discard candidates rejected by the segmentation algorithm ($n_s = 0$), we also sought to retain those with significant IC (IC>100), specifically the

blue candidates falling in the IC>100 range despite $n_s = 0$. These blue candidates are illustrated in the [Figure 5](#) (top), while the green and red candidates are presented in the middle and bottom sections, respectively, of [Figure 4](#).

Despite recommending the removal of all red candidates in the top 1000 candidates from the BG sample, we recognized a potential loss of three democratically selected red candidates. The total count of these democratically selected candidates in [Figure 4](#) (right) is 41, distributed as 3 red, 6 blue, 6 green, and 26 yellow candidates. Notably, the proposed removal strategy would result in only a ~ 7% loss, specifically three red candidates. Therefore, our validation of segmentation algorithm, based on the votes from human classifiers, underscores that eliminating red candidates can significantly reduce false positives in the final sample by approximately a quarter, without losing confirmable strong lensing candidates.

We also have found four strong lensing candidates in the BG sample which have not been previously discovered before. These candidates have been voted as lens or may-be lens by four or more human classifiers. The candidates are shown in [Figure 9](#).

4.3 LRG sample

We repeated the experiment with the LRG sample and we fed the LRG samples to U-Denselens network. We performed the voting with the human classifiers again for the top-200 candidates (based on P_{mean}) out of ~ 126000 candidates.

We carried out the voting experiment for the LRG sample with the decision tree implemented in [Sec. 4.2](#). The mean of human classifier votes s_m is plotted against P_{mean} . This is shown in [Figure 6](#) (left). There were 9, 116, 52 and 23 candidates in green, yellow, red and blue regimes respectively. The democratically selected candidates are shown in right side of the same figure. We see that none of the red candidates are present in the democratically selected regime. There are five blues and seven yellow candidates in the democratically elected regime which are shown in [Figure 7](#). Out of the total 200 candidates, by removing all the 52 red candidates we again can reduce the false positives in the total sample by a quarter. The standard deviation for many candidates are high showing high disagreement among voters for certain candidates. The candidates having highest standard deviation is shown in [Figure 8](#) and their details in [Table D4](#). This shows that these candidates show lensing features that does not convince all of the voters. We once again apply the decision tree and show that we can reduce the final automated sample by ~ 25% by combining the results from P_{mean} , IC_{mean} and n_s in the LRG sample.

5 DISCUSSION

The primary objective of this paper is to develop a fully automated algorithm capable of classifying strong lenses without requiring human vetting, particularly in extensive surveys like Euclid, dealing with datasets comprising several million candidates. Previous approaches in strong lens classification have predominantly relied on the classification probability (P). In our prior work, 'Denselens' [Nagam et al. \(2023\)](#), we introduced the concept of combining 'P' and 'IC' (Intensity Contrast) to refine candidate selection. After filtering based on 'P', we rank-order candidates using 'IC.' However, a crucial question arises: Can we differentiate final candidates based on whether they contain pixels belonging to the source? To address

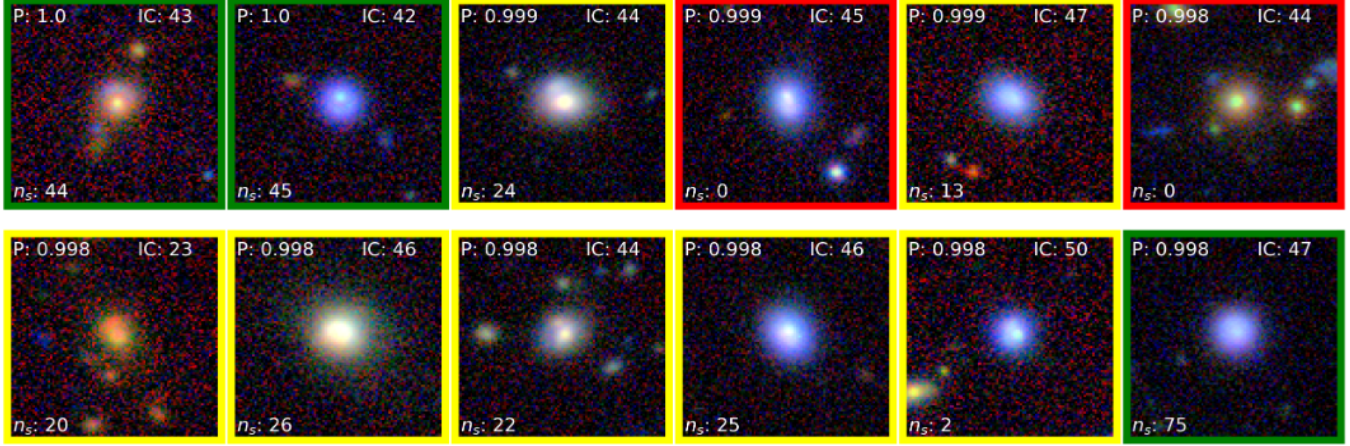


Figure 2. High ranked candidates (based on P) with $IC \leq 50$. Such candidates (including the candidates shown) whose $IC \leq 50$, were removed before given to the human classifiers for voting. Their details are shown in Table D1

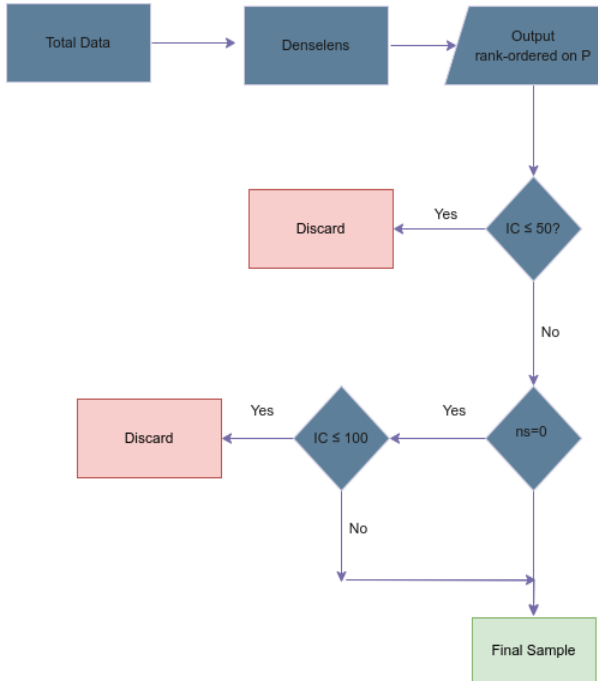


Figure 3. Flow diagram for the selection of strong gravitational lenses explained in 4.2.

this, we introduce segmentation as a means to identify source pixels.

This leads to the second question of whether segmentation information can enhance strong lens classification. Here, we propose the idea of considering the number of pixels (n_s) above a segmentation threshold (S_{thres}) as an additional metric to reduce false positives. 'P,' 'IC,' and n_s are not independent metrics; hence, we employ a decision tree to judiciously combine them. To ensure that the decision tree does not discard confirmable strong lens candidates during the sample size reduction via segmentation, we validate it through voting with human classifiers, confirming the removal of false positives while retaining genuine lenses.

With the decision tree tailored for the BG sample, a pertinent question arises: Can it generalize effectively with different selection

criteria for cutouts? To answer this, we apply the decision tree to an LRG sample, obtaining similar results and demonstrating a substantial removal of false positives, constituting one-fourth of the final sample.

Furthermore, we explore the broader benefits of source pixel segmentation. Subtracting foreground lens light significantly aids lens modeling (Etherington et al. 2022; Nightingale et al. 2018). Previous studies, such as Pearson et al. 2019, have shown a 34% average increase in accuracy by removing foreground lens light. In the future, the segmentation of source pixels holds immense potential as an initial step for lens modeling.

6 CONCLUSION

We introduce the idea of using segmentation algorithm (U-Net) to aid in reducing false positives. We add this U-net algorithm to the pipeline end of our previously published algorithm (Nagam et al. 2023) which primarily used P_{mean} and IC_{mean} to detect and rank-order strong lenses.

We generate a mock dataset of 10,000 lens and 10,000 non-lens instances, we applied a classification threshold ($P_{\text{thres}} > 0.3$), resulting in the identification of 9,586 lens candidates and 875 non-lens candidates. Analyzing the distribution of candidates, especially the impact of the "Red" candidates, revealed a critical trade-off. While excluding candidates in the "Red" candidates could eliminate 77% of false positives, it came at the cost of potentially discarding 14% of true lenses. This highlights the significance of segmentation results, paving way for further reduction in false positives.

The decision tree for the selection of strong gravitational lenses, detailed in the Bright Galaxy (BG) sample, involves rank-ordering candidates based on their classification scores (P), filtering candidates with Information Content (IC) less than or equal to 50, and removing candidates with zero classified source pixels (n_s) and IC values less than or equal to 100. The subsequent human classifier validation process further refines the selection, revealing that eliminating red candidates can significantly reduce false positives without losing confirmable strong lensing candidates. We

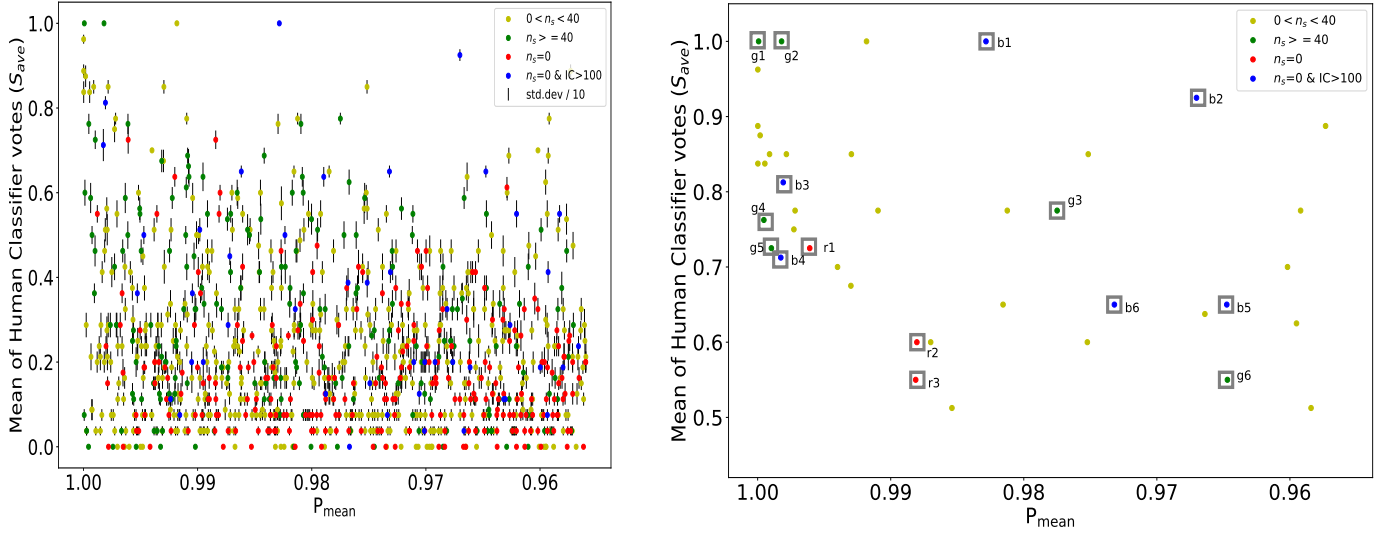


Figure 4. *left:* Mean of human classifier votes (s_m) for all the 1000 candidates with candidate ID rank-ordered based on P . One-tenth of standard deviation of human classifier votes are plotted as black vertical bars. *right:* Candidates which are democratically voted as *May be lens* or *Sure lens* by four or more voters.

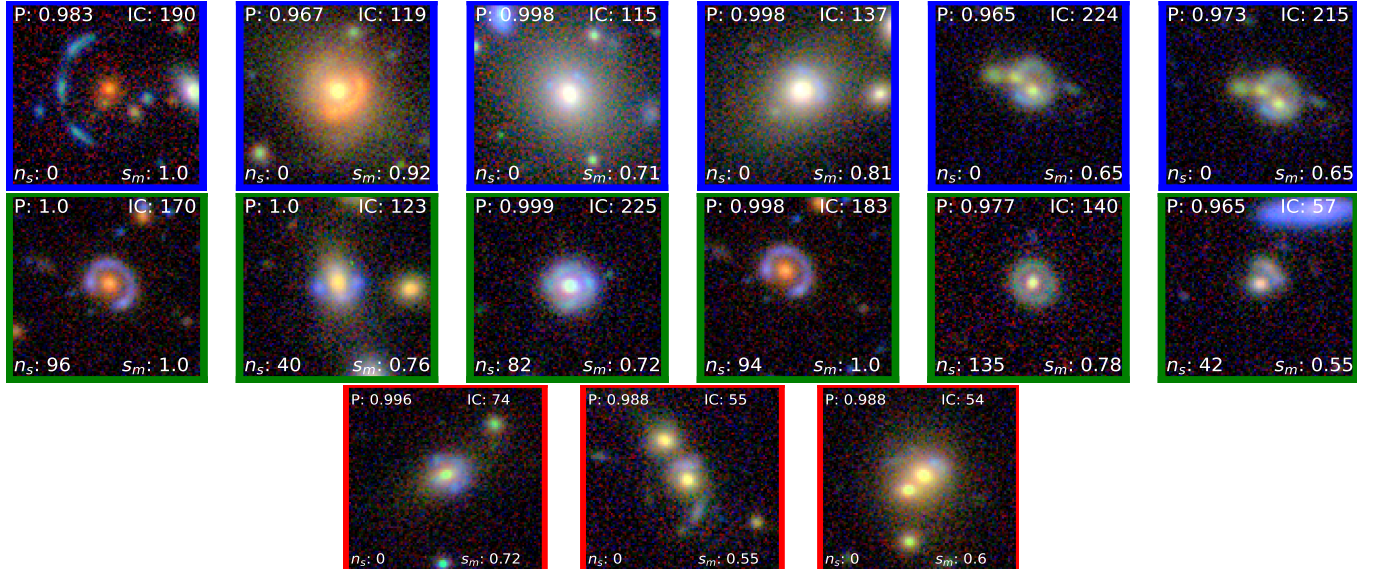


Figure 5. *Top row:* We show the candidates with $n_s=0$ but have $IC>100$ shown as blue points (b1-b6) in Figure 4 (right). *Middle row:* We show the candidates with $n_s>=40$ shown as green points (g1-b6) in Figure 4 (right). *Bottom row:* We show the candidates with $n_s=0$ shown as red points (r1-r6) in Figure 4 (right). Their details are shown in Table D2. The candidates (b5,b6) and (g1,g4) are same candidates but centered on different sources.

present four strong lensing candidates which were discovered with U-Denselens and validated by four or more human classifiers as lens or may-be lens.

The extension of the experiment to the Luminous Red Galaxy (LRG) sample reaffirms the decision tree's effectiveness, demonstrating a reduction in false positives by a quarter. The incorporation of human classifiers in the validation process ensures the preservation of genuine candidates while enhancing the reliability of the selection.

Looking ahead, our study suggests potential avenues for improvement, such as enhancing the realism of training data, incorporating additional lensing types, and expanding the negative database. The proposed decision tree present a robust framework for automation of finding strong gravitational lenses in the upcoming large scale astronomical surveys such as Euclid.

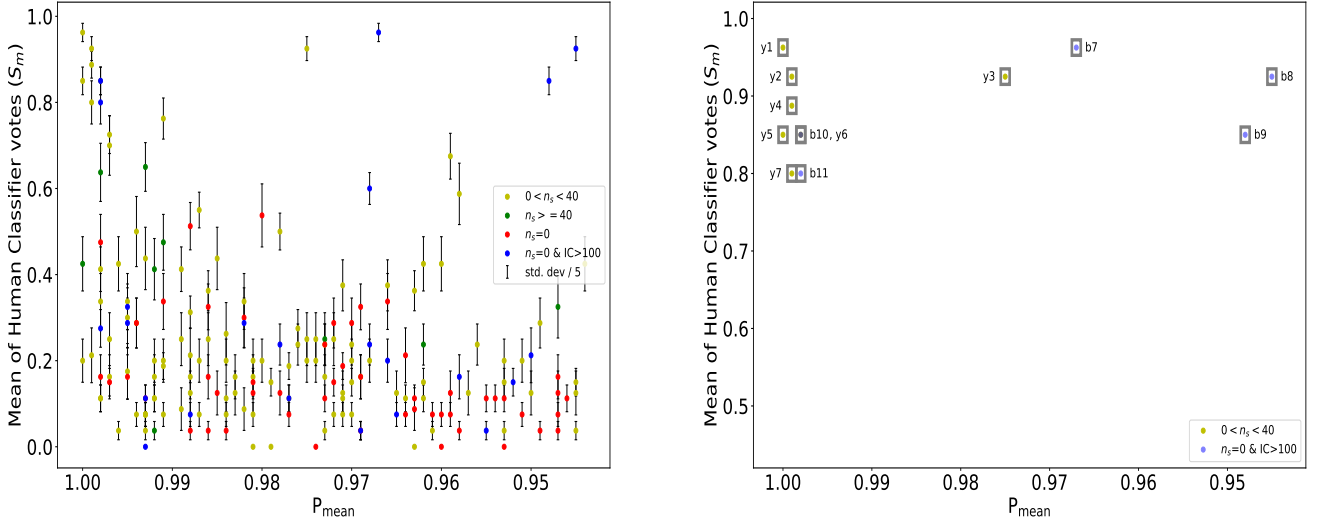


Figure 6. *left:* Mean of human classifier votes (S_m) plotted against P_{mean} . The standard deviation are divided by 5 (for better plotting) and plotted with vertical black lines. Democratically selected candidates

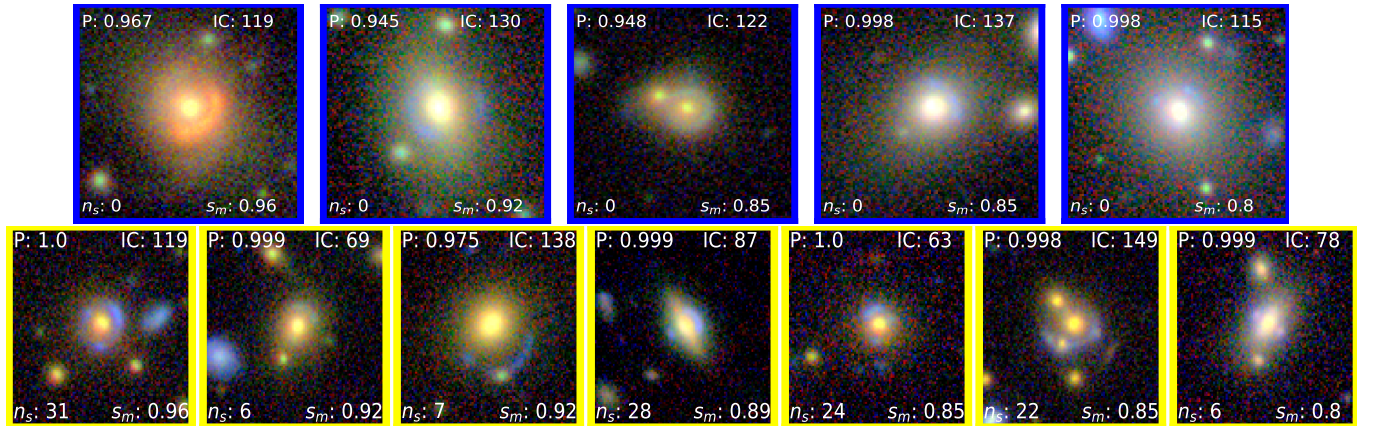


Figure 7. LRG candidates b7-b11 (top) and y1-y7 (bottom) shown in Figure 6 (right). Their details are shown in Table D3.

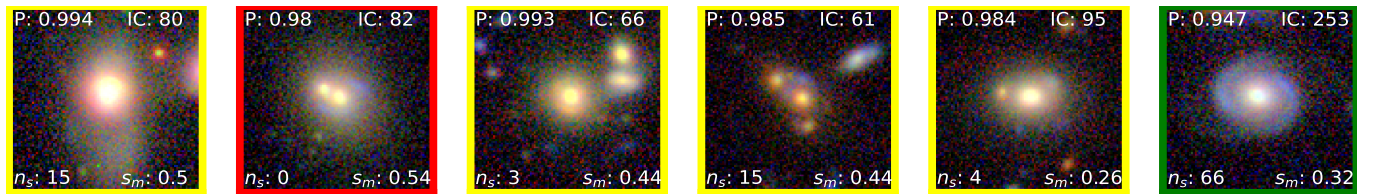


Figure 8. LRG candidates with high standard deviation shown in Figure 6 (left). Their details including standard deviation values s_{std} are shown in Table D4.

ACKNOWLEDGEMENTS

We would like to thank the Center for Information Technology of the University of Groningen for their support and for providing access to the Peregrine high performance computing cluster. The research for this paper was funded by the Centre for Data Science and Systems Complexity at the University of Groningen (www.rug.nl/research/fse/themes/dssc/). We would also thank the collabo-

rators Yue-Dong and Rui Li for creating a website to vote for the lensing candidates.

DATA AVAILABILITY

The data used in the paper is available on request. The data underlying this article will be shared on reasonable request to the corresponding author.

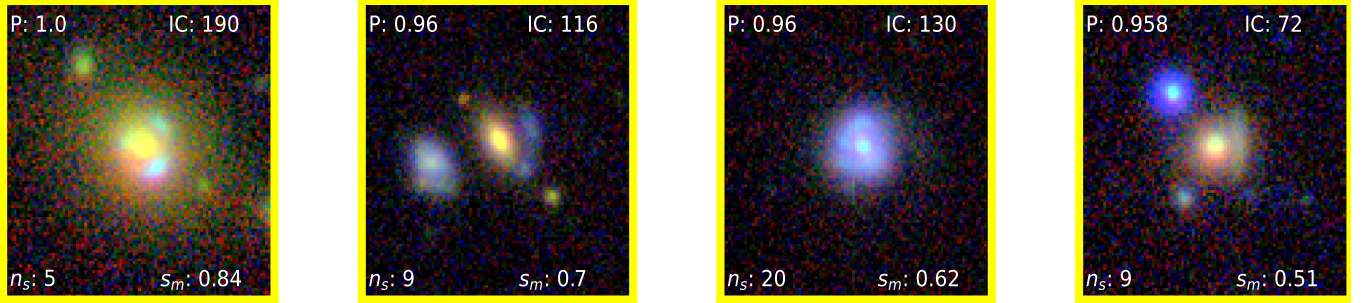


Figure 9. Four new strong lensing candidates discovered in BG sample which have been agreed by four or more human classifiers as lens or may be lens. The details are shown in Table D5.

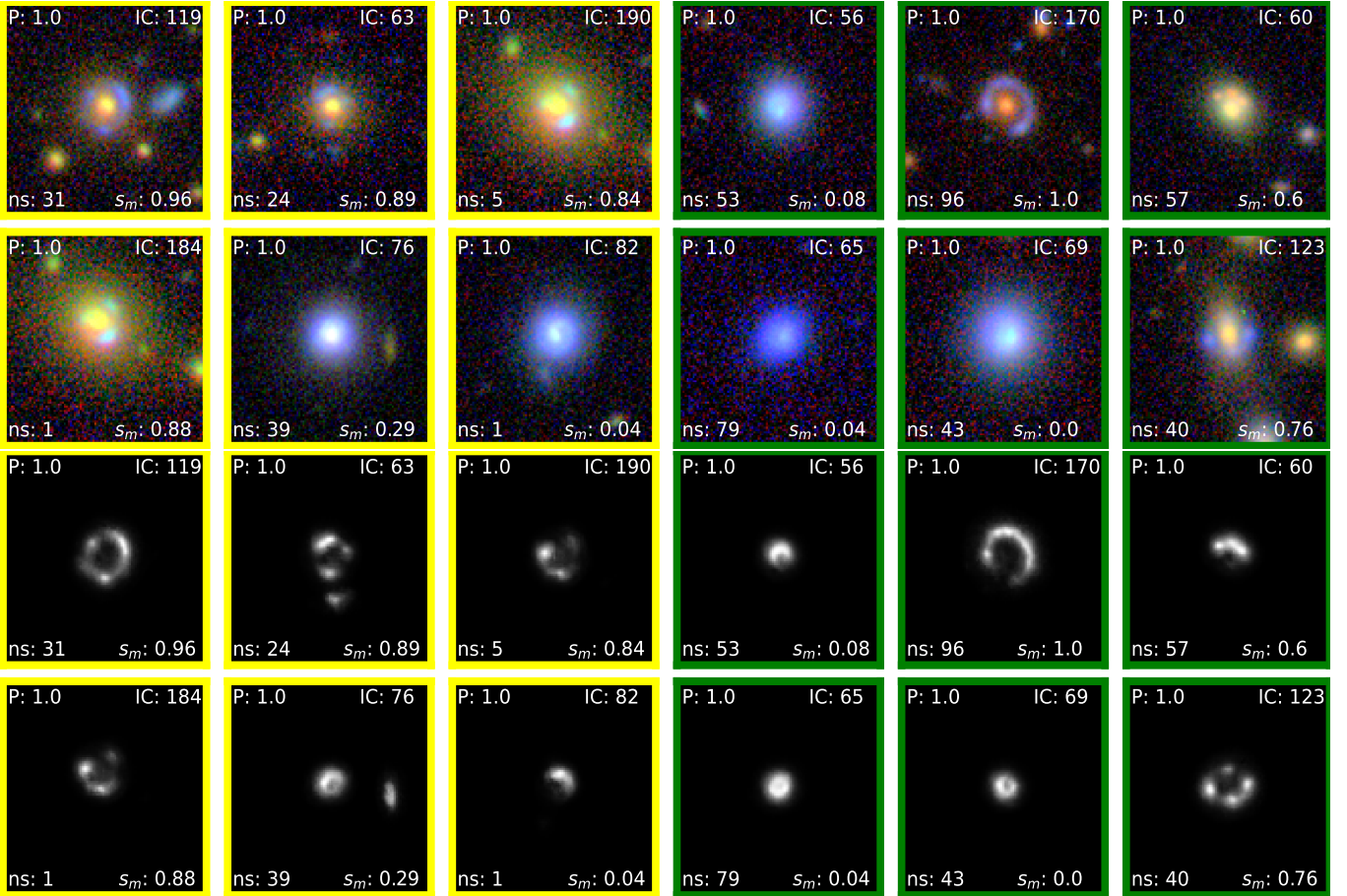


Figure 10. (**Top 2 rows**) Top 12 candidates from BG sample rank-ordered based on P. (**Bottom 2 rows**) Segmentation maps of the corresponding top 12 candidates. We have shown the candidates with n_s scores ≥ 40 with the border green and the candidates between n_s scores > 0 and n_s scores < 40 with the image border yellow. The details are shown in Table D6.

REFERENCES

- Agnello A., et al., 2015, *Monthly Notices of the Royal Astronomical Society*, 454, 1260
- Akeret J., Chang C., Lucchi A., Refregier A., 2017, *Astronomy and Computing*, 18, 35
- Akhazhanov A., et al., 2022, *Monthly Notices of the Royal Astronomical Society*, 513, 2407
- Anguita T., et al., 2018, *Monthly Notices of the Royal Astronomical Society*, 480, 5017
- Badrinarayanan V., Kendall A., Cipolla R., 2017, *IEEE Transactions on Pattern Analysis and Machine Intelligence*, 39, 2481
- Barbera F. L., de Carvalho R. R., Kohl-Moreira J. L., Gal R. R., Soares-Santos M., Capaccioli M., Santos R., Sant'Anna N., 2008, *Publications of the Astronomical Society of the Pacific*, 120, 681
- Barnacka A., 2018, *Physics Reports*, 778, 1
- Bekki K., 2021, *A&A*, 647, A120
- Belokurov V., Evans N., Hewett P., Moiseev A., McMahon R., Sanchez S., King L., 2009, *Monthly Notices of the Royal Astronomical Society*, 392, 104
- Bertin E., Arnouts S., 1996, *Astronomy and astrophysics supplement series*, 117, 393

- Biesiada M., 2006, *Phys. Rev. D*, 73, 023006
- Bolton A. S., Burles S., Koopmans L. V. E., Treu T., Moustakas L. A., 2006a, *The Astrophysical Journal*, 638, 703
- Bolton A. S., Burles S., Koopmans L. V., Treu T., Moustakas L. A., 2006b, *The Astrophysical Journal*, 638, 703
- Bolton A. S., Burles S., Koopmans L. V. E., Treu T., Gavazzi R., Moustakas L. A., Wayth R., Schlegel D. J., 2008, *The Astrophysical Journal*, 682, 964
- Boucaud A., et al., 2019, *Monthly Notices of the Royal Astronomical Society*, 491, 2481
- Browne I., et al., 2003, *Monthly Notices of the Royal Astronomical Society*, 341, 13
- Burke C. J., Aleo P. D., Chen Y.-C., Liu X., Peterson J. R., Sembroski G. H., Lin J. Y.-Y., 2019, *Monthly Notices of the Royal Astronomical Society*, 490, 3952
- Cañámeras, R. et al., 2021, *A&A*, 653, L6
- Cabanac, R. A. et al., 2007, *A&A*, 461, 813
- Cañámeras R., et al., 2020, *Astronomy & Astrophysics*, 644, A163
- Cao Z., Yi Z., Pan J., Su H., Bu Y., Kong X., Luo A., 2023, *The Astronomical Journal*, 165, 184
- Capaccioli M., Schipani P., 2011, *The Messenger*, 146, 27
- Chae K.-H., et al., 2002, *Physical Review Letters*, 89, 151301
- Chae K.-H., Chen G., Ratra B., Lee D.-W., 2004, *The Astrophysical Journal*, 607, L71
- Chan J. H. H., Suyu S. H., Chiueh T., More A., Marshall P. J., Coupon J., Oguri M., Price P., 2015, *The Astrophysical Journal*, 807, 138
- Chan J. H. H., et al., 2016, *The Astrophysical Journal*, 832, 135
- Christ C., Nord B., Gozman K., Ottenbreit K., 2020, in *American Astronomical Society Meeting Abstracts# 235*. pp 303–03
- Collaboration T. D. E. S., 2005, arXiv:astro-ph/0510346, 803, 2
- Collett T. E., 2015, *The Astrophysical Journal*, 811, 20
- Davies A., 2022, PhD thesis, The Open University
- Davies A., Serjeant S., Bromley J. M., 2019, *Monthly Notices of the Royal Astronomical Society*, 487, 5263
- de Jong J. T., Verdoes Kleijn G. A., Kuijken K. H., Valentijn E. A., 2013, *Experimental Astronomy*, 35, 25
- Dewdney P. E., Hall P. J., Schilizzi R. T., Lazio T. J. L. W., 2009, *Proceedings of the IEEE*, 97, 1482
- Diehl H. T., et al., 2017, *The Astrophysical Journal Supplement Series*, 232, 15
- Ellis R. S., 2010, *Philosophical Transactions of the Royal Society A: Mathematical, Physical and Engineering Sciences*, 368, 967
- Etherington A., et al., 2022, *Monthly Notices of the Royal Astronomical Society*, 517, 3275
- Farias H., Ortiz D., Damke G., Jaque Arancibia M., Solar M., 2020, *Astronomy and Computing*, 33, 100420
- Gavazzi R., Treu T., Rhodes J. D., Koopmans L. V. E., Bolton A. S., Burles S., Massey R. J., Moustakas L. A., 2007, *The Astrophysical Journal*, 667, 176
- Gavazzi R., Treu T., Koopmans L. V. E., Bolton A. S., Moustakas L. A., Burles S., Marshall P. J., 2008, *The Astrophysical Journal*, 677, 1046
- Gavazzi R., Marshall P. J., Treu T., Sonnenfeld A., 2014, *The Astrophysical Journal*, 785, 144
- Gentile F., et al., 2021, *Monthly Notices of the Royal Astronomical Society*, 510, 500
- Gilman D., Du X., Benson A., Birrer S., Nierenberg A., Treu T., 2019, *Monthly Notices of the Royal Astronomical Society: Letters*, 492, L12
- Giusarma E., Hurtado M. R., Villaescusa-Navarro F., He S., Ho S., Hahn C., 2019, Learning neutrino effects in Cosmology with Convolutional Neural Networks (arXiv:1910.04255)
- Grillo C., et al., 2018, *The Astrophysical Journal*, 860, 94
- Gu M., Wang F., Hu T., Yu S., 2023, in 2023 4th International Conference on Computer Engineering and Application (ICCEA). pp 512–515, doi:10.1109/ICCEA58433.2023.1013537
- Guo D., Qiu B., Liu Y., Xiang G., 2021, in 2021 6th International Conference on Intelligent Computing and Signal Processing (ICSP). pp 985–988, doi:10.1109/ICSP51882.2021.9409015
- He K., Gkioxari G., Dollár P., Girshick R. B., 2017, CoRR, abs/1703.06870
- He Q., et al., 2020a, *Monthly Notices of the Royal Astronomical Society*, 496, 4717
- He Z., et al., 2020b, *Monthly Notices of the Royal Astronomical Society*, 497, 556
- Heymans C., et al., 2012, *Monthly Notices of the Royal Astronomical Society*, 427, 146
- Huang X., et al., 2020, *The Astrophysical Journal*, 894, 78
- Ibata R. A., et al., 2017, *The Astrophysical Journal*, 848, 128
- Inada N., Oguri M., Rusu C. E., Kayo I., Morokuma T., 2014, *The Astronomical Journal*, 147, 153
- Jacobs C., Glazebrook K., Collett T., More A., McCarthy C., 2017, *Monthly Notices of the Royal Astronomical Society*, 471, 167
- Jaelani A. T., et al., 2020, *Monthly Notices of the Royal Astronomical Society*, 494, 3156
- Jia P., Liu Q., Sun Y., 2020, *The Astronomical Journal*, 159, 212
- Kochanek C. S. P. L. S., 2003, *Carnegie Observatories Astrophysics Series*, 2, 211
- Koopmans L. V. E., 2004, Gravitational Lensing Stellar Dynamics: Dark-Matter and Baryons in Early-type Galaxies to z=1 (arXiv:astro-ph/0412596)
- Koopmans L., Browne I., Jackson N., 2004, *New Astronomy Reviews*, 48, 1085
- Koopmans L. V. E., et al., 2009, *ApJ*, 703, L51
- Kuijken K., et al., 2011, *The Messenger*, 146
- Kuijken K., et al., 2019, *Astronomy & Astrophysics*, 625, A2
- Lanusse F., Ma Q., Li N., Collett T. E., Li C.-L., Ravanbakhsh S., Mandelbaum R., Póczos B., 2018, *Monthly Notices of the Royal Astronomical Society*, 473, 3895
- Laureijs R. J., Duvet L., Sanz I. E., Gondoin P., Lumb D. H., Oosterbroek T., Criado G. S., 2010, in Jr. J. M. O., Clampin M. C., MacEwen H. A., eds, Vol. 7731, Space Telescopes and Instrumentation 2010: Optical, Infrared, and Millimeter Wave. SPIE, pp 453–458, doi:10.1117/12.857123, https://doi.org/10.1117/12.857123
- Lecun Y., Bottou L., Bengio Y., Haffner P., 1998, *Proceedings of the IEEE*, 86, 2278
- Lemon C., et al., 2020, *Monthly Notices of the Royal Astronomical Society*, 494, 3491
- Li R. e. a., 2020, *ApJ*, 899, 30
- Li R., Shu Y., Wang J., 2018, *Monthly Notices of the Royal Astronomical Society*, 480, 431
- Li R., et al., 2020, *The Astrophysical Journal*, 899, 30
- Li R., et al., 2021, High-quality strong lens candidates in the final Kilo Degree survey footprint (arXiv:2110.01905)
- Long M., Yang Z., Xiao J., Yu C., Zhang B., 2019, in *Astronomical Data Analysis Software and Systems XXVII*, Astronomical Society of the Pacific Conference Series. p. 123
- Meneghetti Bartelmann, M. Dolag, K. Moscardini, L. Perrotta, F. Baccigalupi, C. Tormen, G. 2005, *A&A*, 442, 413
- Metcalf et al., 2019, *A&A*, 625, A119
- Mitchell J. L., Keeton C. R., Frieman J. A., Sheth R. K., 2005, *The Astrophysical Journal*, 622, 81
- Miyazaki S., et al., 2012, in McLean I. S., Ramsay S. K., Takami H., eds, Vol. 8446, *Ground-based and Airborne Instrumentation for Astronomy IV*. SPIE, pp 327 – 335, doi:10.1117/12.926844, https://doi.org/10.1117/12.926844
- More A., Cabanac R., More S., Alard C., Limousin M., Kneib J.-P., Gavazzi R., Motta V., 2012, *The Astrophysical Journal*, 749, 38
- More A., et al., 2015, *Monthly Notices of the Royal Astronomical Society*, 455, 1191
- More A., et al., 2016, *Monthly Notices of the Royal Astronomical Society*, 465, 2411
- Myers S., et al., 1999, *The Astronomical Journal*, 117, 2565
- Myers S. T., et al., 2001, in *Gravitational Lensing: Recent Progress and Future Goals*.
- Nadler E. O., Birrer S., Gilman D., Wechsler R. H., Du X., Benson A., Nierenberg A. M., Treu T., 2021, *The Astrophysical Journal*, 917, 7
- Nagam B. C., Koopmans L. V. E., Valentijn E. A., Kleijn G. V., de Jong J. T. A., Napolitano N., Li R., Tortora C., 2023, *Monthly Notices of the*

- Royal Astronomical Society, 523, 4188
- Narayan S., 1997, *Information Sciences*, 99, 69
- Nightingale J. W., Dye S., Massey R. J., 2018, *Monthly Notices of the Royal Astronomical Society*, 478, 4738
- Nightingale J. W., Massey R. J., Harvey D. R., Cooper A. P., Etherington A., Tam S.-I., Hayes R. G., 2019, *Monthly Notices of the Royal Astronomical Society*, 489, 2049
- Nord B., Buckley-Geer E. J., Lin H., Diehl H. T., Gaitsch H., 2015, [225, 255.21](#)
- Nord B., et al., 2016, *The Astrophysical Journal*, 827, 51
- Nord B., et al., 2020, *Monthly Notices of the Royal Astronomical Society*, 494, 1308
- Oguri M., et al., 2005, *The Astrophysical Journal*, 622, 106
- Oguri M., et al., 2006, [AJ, 132, 999](#)
- Oguri M., et al., 2008a, *The Astronomical Journal*, 135, 512
- Oguri M., et al., 2008b, [AJ, 135, 520](#)
- Ostdiek, Bryan Diaz Rivero, Ana Dvorkin, Cora 2022a, [A&A, 657, L14](#)
- Ostdiek, Bryan Diaz Rivero, Ana Dvorkin, Cora 2022b, *The Astrophysical Journal*, 927, 83
- O'Donnell J. H., et al., 2022, *The Astrophysical Journal Supplement Series*, 259, 27
- Pawase R. S., Courbin F., Faure C., Kokotanekova R., Meylan G., 2014, *Monthly Notices of the Royal Astronomical Society*, 439, 3392–3404
- Pearson Pennock, Clara Robinson, Tom 2018, *Emergent Scientist*, 2, 1
- Pearson J., Li N., Dye S., 2019, *Monthly Notices of the Royal Astronomical Society*, 488, 991
- Petrillo C. E., et al., 2017, *Monthly Notices of the Royal Astronomical Society*, 472, 1129
- Petrillo C. E., et al., 2019a, *Monthly Notices of the Royal Astronomical Society*, 482, 807
- Petrillo C. E., et al., 2019b, *Monthly Notices of the Royal Astronomical Society*, 484, 3879
- Pourrahmani M., Nayyeri H., Cooray A., 2018, *The Astrophysical Journal*, 856, 68
- Qi J., Chen M., Wu Z., Su C., Yao X., Mei C., 2022, in 2022 China Automation Congress (CAC). pp 1901–1905, doi:[10.1109/CAC57257.2022.10054887](#)
- Quinn P., Axelrod T., Bird I., Dodson R., Szalay A., Wicenec A., 2015, arXiv preprint arXiv:1501.05367
- Ren S., He K., Girshick R., Sun J., 2015, in Cortes C., Lawrence N., Lee D., Sugiyama M., Garnett R., eds, Vol. 28, Advances in Neural Information Processing Systems. Curran Associates, Inc., https://proceedings.neurips.cc/paper_files/paper/2015/file/14bfa6bb14875e45bba028a21ed38046-Paper.pdf
- Rezaei S., McKean J., Biehl M., de W., Lafontaine A., 2022
- Rhee G., 1991, *Nature*, 350, 211
- Riggi S., et al., 2023, *Astronomy and Computing*, 42, 100682
- Rojas K., et al., 2021, Strong lens systems search in the Dark Energy Survey using Convolutional Neural Networks ([arXiv:2109.00014](#))
- Ronneberger O., Fischer P., Brox T., 2015, U-Net: Convolutional Networks for Biomedical Image Segmentation ([arXiv:1505.04597](#))
- Sarbu N., Rusin D., Ma C.-P., 2001, *The Astrophysical Journal*, 561, L147
- Savary E., et al., 2021
- Savary E., et al., 2022, *Astronomy & Astrophysics*, 666, A1
- Schaefer C., Geiger M., Kuntzer T., Kneib J.-P., 2018, *Astronomy & Astrophysics*, 611, A2
- Sereno 2002, [A&A, 393, 757](#)
- Serjeant S., 2014, *The Astrophysical Journal*, 793, L10
- Shu, Yiping Cañameras, Raoul Schuldt, Stefan Suyu, Sherry H. Taubenberger, Stefan Inoue, Kaiki Taro Jaelani, Anton T. 2022, [A&A, 662, A4](#)
- Shu Bolton A. S., Brownstein J. R., 2015, *The Astrophysical Journal*, 803, 2
- Shu Brownstein J. R., Bolton A. S., Koopmans L. V. E., 2017, *The Astrophysical Journal*, 851, 48
- Simpson R., Page K. R., De Roure D., 2014, in Proceedings of the 23rd international conference on world wide web. pp 1049–1054
- Spinelli C., Barnabè M., Koopmans L. V. E., Trager S. C., 2015, *Monthly Notices of the Royal Astronomical Society: Letters*, 452, L21
- Sygnat, J. F. Tu, H. Fort, B. Gavazzi, R. 2010, [A&A, 517, A25](#)
- Tanaka M., et al., 2016, *The Astrophysical Journal Letters*, 826, L19
- Tanoglidis D., et al., 2022, *Astronomy and Computing*, 39, 100580
- Treu T., Ellis R. S., 2015, *Contemporary Physics*, 56, 17
- Treu T., Koopmans L. V. E., 2002, *The Astrophysical Journal*, 575, 87
- Treu T., Shajib A. J., 2023, Strong Lensing and H_0 ([arXiv:2307.05714](#))
- Treu T., et al., 2018, *Monthly Notices of the Royal Astronomical Society*, 481, 1041
- Treu T., Suyu S. H., Marshall P. J., 2022, *The Astronomy and Astrophysics Review*, 30, 8
- Turner E. L., Ostriker J. P., Gott III J. R., 1984, *The Astrophysical Journal*, 284, 1
- Turyshev S. G., Toth V. T., 2022, *Monthly Notices of the Royal Astronomical Society*, 513, 5355
- Tyson J. A., 2002, in Tyson J. A., Wolff S., eds, Vol. 4836, Survey and Other Telescope Technologies and Discoveries. SPIE, pp 10 – 20, doi:[10.1117/12.456772](#), <https://doi.org/10.1117/12.456772>
- Vojtěkova A., Lieu M., Valtchanov I., Altieri B., Old L., Chen Q., Hroch F., 2020, *Monthly Notices of the Royal Astronomical Society*, 503, 3204
- Wang Y., et al., 2022, *The Astrophysical Journal*, 928, 1
- Weiner C., Serjeant S., Sedgwick C., 2020, *Research Notes of the AAS*, 4, 190
- Widyaningrum R., Candradewi I., Aji N. R. A. S., Aulianisa R., 2022, *Imaging Science in Dentistry*, 52, 383
- Wong K., HSC SSP Strong Lens Working Group 2018, in American Astronomical Society Meeting Abstracts #231. p. 226.01
- Wu T., 2020, in 2020 International Conference on Big Data Artificial Intelligence Software Engineering (ICBASE). pp 390–393, doi:[10.1109/ICBASE51474.2020.00089](#)
- Wu C., et al., 2018, *Monthly Notices of the Royal Astronomical Society*, 482, 1211
- Zhan H., 2018, 42nd COSPAR Scientific Assembly, 42, E1
- Zhang T.-J., 2004, *The Astrophysical Journal*, 602, L5
- Zitrin A., et al., 2012, *The Astrophysical Journal*, 749, 97
- Şengül A., Dvorkin C., 2022, *Monthly Notices of the Royal Astronomical Society*, 516, 336

APPENDIX A: SEGMENTATION TRAINING

The U-Net algorithm is trained for positive candidates (lenses) with source pixels as 1 and the rest of the pixels as 0. This is explained in [Figure A1](#) (top). For non-lenses, all the pixels are trained with label 0 as shown in [Figure A1](#) (bottom). Our training data set comprised of positive samples (mock lenses) generated from 100,000 samples and ~ 6000 non-lenses (refer [Nagam et al. 2023](#)) for training, testing and validation. We have trained a single U-Net network (not an ensemble) for about 2500 iterations. Our batch size for each training comprised of 64 samples for training and 32 samples for validation.

APPENDIX B: MOCK LENSES

We have shown a sample of mock lenses used in the research. [Figure 8](#) (top) and (bottom) shows the top 25 rank-ordered candidates and its respective segmentation maps from the mock data.

APPENDIX C: OTHER APPROACHES

We conducted an experiment involving a four-CNN network ensemble, utilizing segmentation maps instead of traditional images, to assess the potential performance improvements with this alternative input. Surprisingly, our findings revealed a decrease in performance when the networks were trained with segmentation maps. This leads us to the conclusion that CNNs trained on segmentation maps may

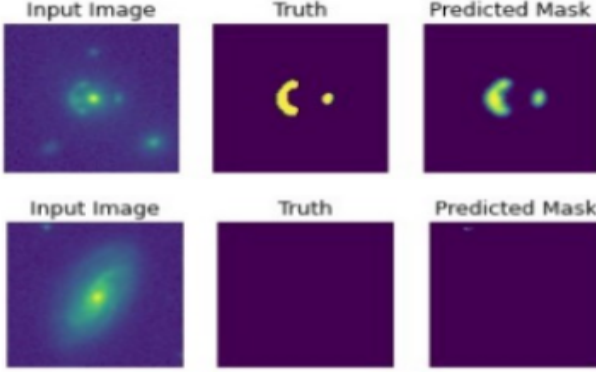


Figure A1. The training of lenses and non-lenses for the U-Net algorithm. For training, the source pixels are labelled as 1 and rest of the pixels are labelled as 0 (top). For non-lenses, all the pixels are labelled as 0 for the training (below).

KiDS tile name	RA	DEC	P	IC	n_s
KIDS_204.0_0.5	203.747796	0.271528	0.99967	43.30	44
KIDS_195.0_0.5	194.710143	-0.224885	0.99960	41.66	45
KIDS_349.6_-30.2	350.173666	-30.600492	0.99945	43.79	24
KIDS_335.5_-31.2	335.055485	-31.259669	0.99886	44.76	0
KIDS_231.0_0.5	231.114952	0.838905	0.99860	46.60	13
KIDS_33.6_-34.1	33.98169	-34.407147	0.99846	43.73	0
KIDS_25.1_-29.2	24.558549	-29.430491	0.99832	22.60	20
KIDS_353.2_-29.2	353.474196	-29.531741	0.99809	46.35	26
KIDS_46.7_-29.2	46.272839	-29.246367	0.99802	43.61	22
KIDS_24.0_-34.1	24.492328	-33.998216	0.99801	45.72	25
KIDS_222.6_2.5	222.580281	2.125373	0.99797	49.78	2
KIDS_349.7_-29.2	349.463897	-29.616792	0.99783	46.88	75

TABLE D1: KiDS tile name, RA, DEC, P, IC and n_s values for the candidates with IC ≤ 50 shown in Figure 2

struggle due to the inherently reduced information content compared to original cutout images.

It is evident that the CNNs trained on original cutouts exhibit superior learning capabilities, capturing additional crucial information such as lens properties, background objects within the field, and their respective intensities. This underscores the importance of utilizing original cutout images for training, as they provide a richer dataset for the networks to learn and comprehend the complexities of the visual data at hand.

APPENDIX D: TABLES

In this section, we primarily show the KiDS tile name, RA, DEC, P, IC and n_s values for the candidates displayed in Sec 4

This paper has been typeset from a TeX/LaTeX file prepared by the author.

KiDS tile name	RA	DEC	P	IC	n_s	tag
KIDS_16.3_-31.2	16.770493	-31.478064	0.98284	190	0	b1
KIDS_130.0_-1.5	129.889052	-1.679115	0.96702	119	0	b2
KIDS_182.0_-1.5	181.93025	-1.065401	0.99826	115	0	b3
KIDS_159.4_-2.5	159.780754	-2.275022	0.99808	137	0	b4
KIDS_11.7_-31.2	11.559175	-31.340792	0.96475	224	0	b5
KIDS_11.7_-31.2	11.559687	-31.340386	0.97319	215	0	b6
KIDS_344.9_-31.2	345.395628	-31.543209	0.99609	74	0	r1
KIDS_2.4_-34.1	2.084894	-34.455275	0.98812	55	0	r2
KIDS_31.2_-34.1	31.476136	-34.338695	0.98804	54	0	r3
KIDS_15.6_-34.1	15.366003	-33.722057	0.99993	170	96	g1
KIDS_345.6_-34.1	345.609561	-33.943769	0.99953	123	40	g2
KIDS_3.5_-31.2	3.020876	-30.684705	0.99897	225	82	g3
KIDS_15.6_-34.1	15.365425	-33.722465	0.99820	183	94	g4
KIDS_216.6_-2.5	216.732485	-2.622653	0.97750	140	135	g5
KIDS_350.5_-33.1	350.712555	-33.181472	0.96470	57	42	g6

TABLE D2: top 12 KiDS tile name, RA, DEC, P, IC and n_s values for the candidates with IC ≤ 50 shown in Figure 5

KiDS tile name	RA	DEC	P	IC	n_s	tag
KIDS_130.0_-1.5	129.889052	-1.679115	0.967	119	0	b7
KIDS_333.9_-33.1	333.412536	-33.198985	0.945	130	0	b8
KIDS_31.2_-34.1	31.619539	-33.796853	0.948	122	0	b9
KIDS_159.4_-2.5	159.780754	-2.275022	0.998	137	0	b10
KIDS_182.0_-1.5	181.93025	-1.065401	0.998	115	0	b11
KIDS_47.1_-27.2	46.66537	-27.607481	1	119	31	y1
KIDS_189.0_0.5	188.97575	0.93067	0.999	69.3	6	y2
KIDS_134.0_-1.5	133.693949	-1.360288	0.975	138	7	y3
KIDS_168.0_0.5	168.224904	0.179072	0.999	87.4	28	y4
KIDS_24.2_-30.2	23.607086	-29.947897	1	62.8	24	y5
KIDS_205.0_-1.5	204.686617	-1.151341	0.998	149	22	y6
KIDS_186.0_0.5	186.233401	0.846682	0.999	77.6	6	y7

TABLE D3: KiDS tile name, RA, DEC, P, IC, n_s and the name tag values for the LRG candidates shown in Figure 7

KiDS tile name	RA	DEC	P	IC	n_s	s_m	s_{std}
KIDS_238.0_-1.5	238.000448	-1.785379	0.994	79.8	15	0.5	0.4071
KIDS_184.0_-0.5	183.600158	-0.535089	0.98	81.5	0	0.5375	0.3662
KIDS_48.9_-31.2	48.819245	-31.131718	0.993	65.9	3	0.4375	0.3623
KIDS_34.5_-33.1	34.78658	-33.52217	0.985	61.3	15	0.4375	0.3623
KIDS_1.2_-34.1	1.569209	-34.476066	0.984	94.6	4	0.2625	0.3623
KIDS_185.0_0.5	185.354352	0.964915	0.947	253	66	0.325	0.3615

TABLE D4: KiDS tile name, RA, DEC, P, IC, n_s , s_m and s_{std} values for high std. dev. candidates of LRG sample shown in Figure 8

KiDS tile name	RA	DEC	P	IC	n_s	s_m
KIDS_2.4_-32.1	2.067021	-32.620669	1	190	5	0.84
KIDS_226.0_-0.5	226.089096	-0.066187	0.96	116	9	0.70
KIDS_4.8_-34.1	5.318212	-33.769457	0.96	130	20	0.62
KIDS_208.0_-0.5	207.860973	-0.199983	0.96	72	9	0.51

TABLE D5: KiDS tile name, RA, DEC, P, IC, n_s , s_m , values for high std. dev. candidates of LRG sample shown in Figure 9

KiDS tile name	RA	DEC	P	IC	n_s	s_m
KIDS_47.1_-27.2	46.66537	-27.607481	0.99999	119	31	0.96
KIDS_24.2_-30.2	23.607086	-29.947897	0.99999	63	24	0.89
KIDS_2.4_-32.1	2.067021	-32.620669	0.99999	190	5	0.84
KIDS_164.0_-0.5	163.792396	-0.68975	0.99994	56	53	0.08
KIDS_15.6_-34.1	15.366003	-33.722057	0.99993	170	96	1.0
KIDS_215.0_-0.5	214.827121	-0.420325	0.99988	60	57	0.6
KIDS_2.4_-32.1	2.066701	-32.621056	0.99981	184	1	0.88
KIDS_30.6_-32.1	31.079838	-32.007072	0.99976	76	39	0.29
KIDS_49.2_-34.1	48.764524	-34.404492	0.99973	82	1	0.04
KIDS_225.0_-0.5	224.895194	-0.407729	0.99973	65	79	0.04
KIDS_42.8_-33.1	42.709956	-33.576519	0.99956	69	43	0
KIDS_345.6_-34.1	345.609561	-33.943769	0.99953	123	40	0.76

TABLE D6: KiDS tile name, RA, DEC, P, IC, n_s , s_m and s_{std} values for high std. dev. candidates of BG sample shown in Figure 10

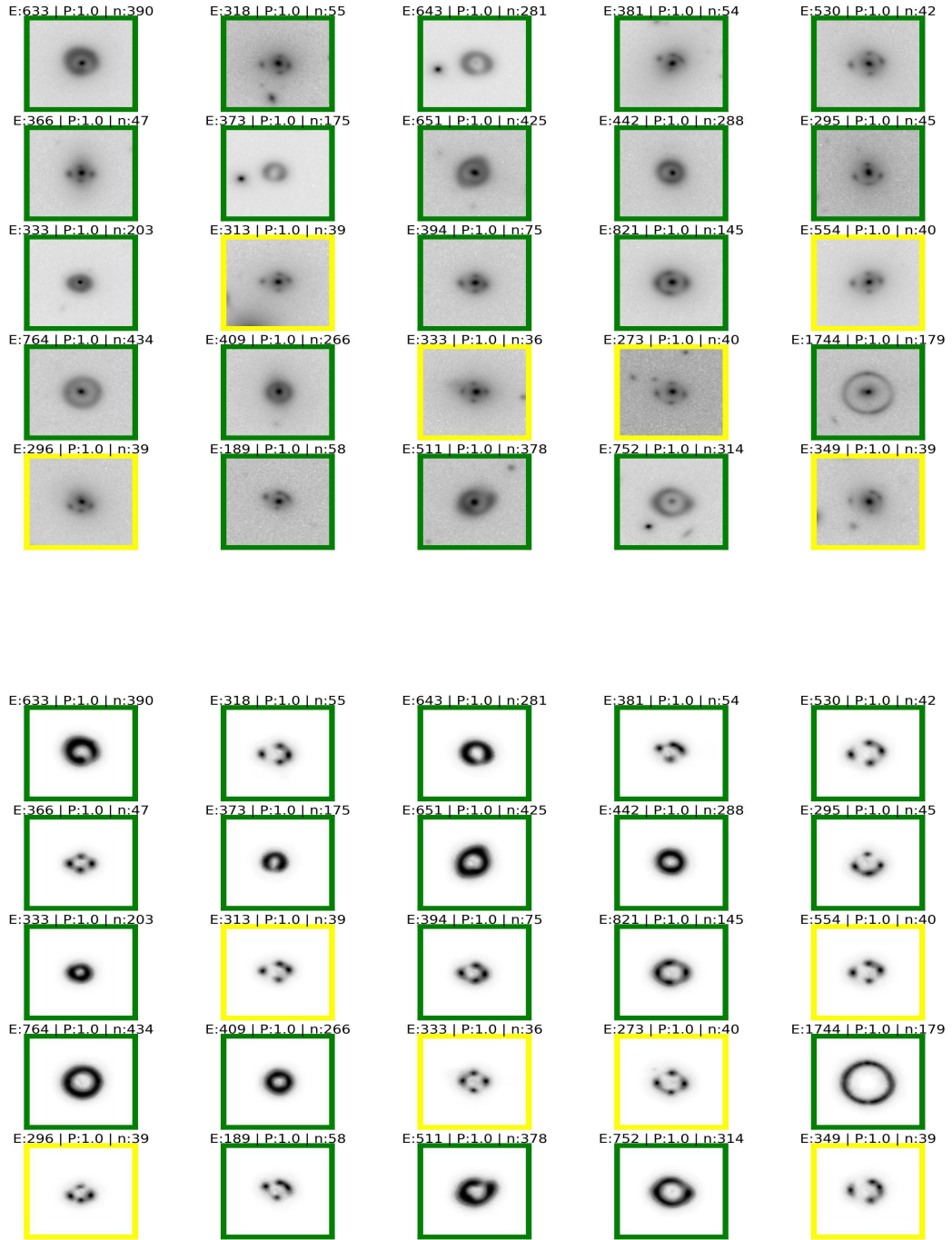


Figure B1. Illustration of DenseLens results for mock data. **Top:** Classification prediction scores (P), IC (E), total number of classified source pixels (n_s) for first 25 candidates ran-ordered by P value. **Bottom:** The bottom plot shows the segmentation results